AFRL-AFOSR-VA-TR-2019-0158

Novel optical techniques for investigating cellular and vascular biophysics

James Fujimoto
MASSACHUSETTS INSTITUTE OF TECHNOLOGY

04/09/2019
Final Report

Air Force Research Laboratory
AF Office Of Scientific Research (AFOSR)/ RTB2
Arlington, Virginia 22203
Air Force Materiel Command

DISTRIBUTION A: Distribution approved for public release.

REPORT DOCUMENTATION PAGE

Form Approved
OMB No. 0704-0188

1. REPORT DATE *(DD-MM-YYYY)*	2. REPORT TYPE	3. DATES COVERED *(From - To)*
21-06-2019	Final Performance	15 Sep 2015 to 14 Sep 2018

4. TITLE AND SUBTITLE
Novel optical techniques for investigating cellular and vascular biophysics

5a. CONTRACT NUMBER

5b. GRANT NUMBER
FA9550-15-1-0473

5c. PROGRAM ELEMENT NUMBER
61102F

6. AUTHOR(S)
James Fujimoto

5d. PROJECT NUMBER

5e. TASK NUMBER

5f. WORK UNIT NUMBER

7. PERFORMING ORGANIZATION NAME(S) AND ADDRESS(ES)
MASSACHUSETTS INSTITUTE OF TECHNOLOGY
77 MASSACHUSETTS AVE
CAMBRIDGE, MA 02139-4301 US

8. PERFORMING ORGANIZATION REPORT NUMBER

9. SPONSORING/MONITORING AGENCY NAME(S) AND ADDRESS(ES)
AF Office of Scientific Research
875 N. Randolph St. Room 3112
Arlington, VA 22203

10. SPONSOR/MONITOR'S ACRONYM(S)
AFRL/AFOSR RTB2

11. SPONSOR/MONITOR'S REPORT NUMBER(S)
AFRL-AFOSR-VA-TR-2019-0158

12. DISTRIBUTION/AVAILABILITY STATEMENT
A DISTRIBUTION UNLIMITED: PB Public Release

13. SUPPLEMENTARY NOTES

14. ABSTRACT
This is a collaborative program between investigators at the Massachusetts Institute of Technology and Massachusetts General Hospital / Boston University to develop new optical imaging technologies and investigate fundamental cellular and vascular biophysical processes. Research themes in this program included: (1) Developing dynamic light scattering (DLS) theory for optical coherence tomography (OCT) imaging to investigate biophysical process of fluid transport and blood flow. (2) Developing OCT angiography (OCTA) and phase-resolved Doppler OCT techniques to investigate the flow mechanics in cerebral and retinal circulation. (3) Developing new OCTA techniques to investigate functional response in the human retina. (4) Developing ultrahigh resolution spectral domain OCT (SD-OCT) techniques to investigate photoreceptor and retinal pigment epithelium function in humans. (5) Developing nonlinear microscopy (NLM) for rapid virtual histology of tissue specimens.

A key focus is to demonstrate these new imaging technologies for studies in the brain and retina. Improved understanding of biophysical processes in the brain is critical for advancing neuroscience as well as developing treatments for traumatic brain injury, stroke and other conditions. Conversely, studies of functional processes in retina are important for fundamental science as well as investigating vision threating diseases such as age related macular degeneration and diabetes. The retina is complimentary to the brain, exhibiting many biophysical features present in the brain such as neurotransduction and neurovascular coupling, while having the powerful advantage that it can be optically imaged non-invasively in humans. An additional theme is the development of techniques for virtual histology, addressing the problem of visualizing cellular structure in intact tissue specimens. This work has the potential to ha

15. SUBJECT TERMS
Optical Coherence Tomography, brain imaging, vascular dynamics

16. SECURITY CLASSIFICATION OF:			17. LIMITATION OF ABSTRACT	18. NUMBER OF PAGES	19a. NAME OF RESPONSIBLE PERSON
a. REPORT	b. ABSTRACT	c. THIS PAGE			BIN-SALAMON, SOFI
Unclassified	Unclassified	Unclassified	UU		19b. TELEPHONE NUMBER *(Include area code)* 703-696-8411

AFOSR Grant Award FA9550-15-1-0473

Title: Novel Optical Techniques for Investigating Cellular and Vascular Biophysics

Final Report (15 September 2015 - 14 September 2018)

Investigators: Co-PI: James G. Fujimoto, Ph.D. Massachusetts Institute of Technology
Co-PI: David Boas, Ph.D. Massachusetts General Hospital and Boston University

AFOSR Program Manager: Sofi Bin-Salamon, Ph.D and William P. Roach, Ph.D.

Abstract:

This is a collaborative program between investigators at the Massachusetts Institute of Technology and Massachusetts General Hospital / Boston University to develop new optical imaging technologies and investigate fundamental cellular and vascular biophysical processes. Research themes in this program included: (1) Developing dynamic light scattering (DLS) theory for optical coherence tomography (OCT) imaging to investigate biophysical process of fluid transport and blood flow. (2) Developing OCT angiography (OCTA) and phase-resolved Doppler OCT techniques to investigate the flow mechanics in cerebral and retinal circulation. (3) Developing new OCTA techniques to investigate functional response in the human retina. (4) Developing ultrahigh resolution spectral domain OCT (SD-OCT) techniques to investigate photoreceptor and retinal pigment epithelium function in humans. (5) Developing nonlinear microscopy (NLM) for rapid virtual histology of tissue specimens.

A key focus is to demonstrate these new imaging technologies for studies in the brain and retina. Improved understanding of biophysical processes in the brain is critical for advancing neuroscience as well as developing treatments for traumatic brain injury, stroke and other conditions. Conversely, studies of functional processes in retina are important for fundamental science as well as investigating vision threating diseases such as age related macular degeneration and diabetes. The retina is complimentary to the brain, exhibiting many biophysical features present in the brain such as neurotransduction and neurovascular coupling, while having the powerful advantage that it can be optically imaged non-invasively in humans. An additional theme is the development of techniques for virtual histology, addressing the problem of visualizing cellular structure in intact tissue specimens. This work has the potential to have a powerful impact in fundamental studies as well as intraoperative guidance for cancer surgery.

Funding for this program was discontinued after year 2. This final report recapitulates many of the results described in the previous annual report. Additional new information is presented on ultrahigh speed optical coherence tomography angiography (OCTA) and rapid virtual histology using nonlinear microscopy (NLM). We also include an updated list of publications and PI accomplishments under this program.

Annual Report AFOSR FA9550-15-1-0473

"Novel Optical Techniques for Investigating Cellular and Vascular Biophysics"

Table of Contents

1. Overview

This is a collaborative program between MIT and MGH to develop new optical imaging technologies and investigate fundamental cellular and vascular biophysical processes. Funding for this program was discontinued after year 2. This final report recapitulates many of the results described in the previous annual report. Additional information is presented on ultrahigh speed optical coherence tomography angiography (OCTA) and rapid virtual histology using nonlinear microscopy (NLM) which was not described in the year 2 report. We also include an updated list of publications and PI accomplishments under this program.

Research themes in this program included (1) Applying dynamic light scattering (DLS) theory to optical coherence tomography (OCT) imaging analysis (DLS-OCT) to investigate the biophysical process of fluid transport and blood flow. (2) Developing OCT angiography (OCTA) and phase-resolved Doppler OCT techniques (PR-OCT) to investigate the flow mechanics in cerebral and retinal circulation. (3) Developing new OCTA techniques to investigate functional response and neurovascular coupling in the human retina. (4) Developing ultrahigh resolution spectral domain OCT (UHR-OCT) techniques to investigate photoreceptor and retinal pigment epithelium function in humans. (5) Developing nonlinear microscopy (NLM) for rapid virtual histology of tissue specimens.

A key focus is to apply these new imaging technologies for studies in the brain and retina. Improved understanding of biophysical processes in the brain is critical for advancing neuroscience as well as developing treatments for traumatic brain injury, stroke and other conditions. Conversely, studies of functional processes in retina are important for fundamental science as well as investigating vision threating diseases such as age related macular degeneration and diabetes. The retina is complimentary to the brain, exhibiting many of the biophysical features

present in the brain such as neurotransduction and neurovascular coupling, while having the powerful advantage that it can be optically imaged non-invasively in humans. An additional theme is the development of techniques for virtual histology, addressing the problem of visualizing cellular structure in intact tissue specimens. This work has the potential to have a powerful impact in fundamental studies as well as intraoperative guidance for cancer surgery.

We have also translated technologies and methods developed under this and other AFOSR sponsored programs to perform feasibility studies in retinal disease, endoscopy and surgical guidance. Related publications from this translational research are cited in this report. There are a total of more than 30 peer reviewed journal publications under this program.

2. Rapid virtual histology of tissue specimens using nonlinear microscopy (NLM)

Paraffin embedded histology using transmission light microscopy is the most widely used technique for investigating the cellular and architectural morphology of tissue and has applications ranging from fundamental studies of cells and tissues to cancer diagnosis and intraoperative surgical guidance. However standard histology is time intensive, requiring several hours to days, because tissue specimens must be fixed in formalin, processed, paraffin embedded, microtomed into thin sections, transferred to glass slides and stained before they can be examined with transmission light microscopy. Stains with selective binding or molecular specificity enable specific cellular structures or molecular targets to be visualized. Frozen section analysis (FSA) reduces the processing time by rapidly freezing tissue in an embedding agent to enable cryotoming into thin sections which are then transferred to slides and stained. FSA can be performed in ~20 minutes, however the size of the tissue is limited because of the difficulty in cryosectioning large specimens and specimens must be processed individually in a serial fashion, limiting the area that can be examined. The development of techniques which can generate histology like images of tissue with cellular resolution, but in real time, without the need to physically section the tissue into thin slices would accelerate fundamental research as well as enable many new applications in surgical guidance.

The approach to this problem is grounded in biophysics, with the key challenge being visualization of cellular and subcellular structures such as the nucleus in intact tissue. These studies involve excised tissues, while the other program topics focus on in vivo imaging. We report these studies first because they were not highlighted in the previous report and they have the potential to have a high impact with powerful translational implications for surgical guidance in breast and prostate cancer surgery.

Working with pathologists and surgeons at the Beth Israel Deaconess Medical Center (BIDMC) / Harvard Medical School, we have been developing and investigating nonlinear microscopy (NLM) to perform real time virtual histology. NLM uses a scanned ultrashort pulse laser to nonlinearly excite fluorescence at the laser focus, generating an optical sectioning effect. Tissue specimens can be rapid stained with selectively binding fluorescent agents and large regions rapidly imaged in real time. We demonstrated real-time histological evaluation of cancer surgical specimens by staining with acridine orange (AO) for nuclear contrast and sulforhodamine 101 (SR101) for

stromal contrast analogous to hematoxylin and eosin (H&E), imaging specimens with a fluorescence NLM using a compact femtosecond fiber laser (Fig. 1).

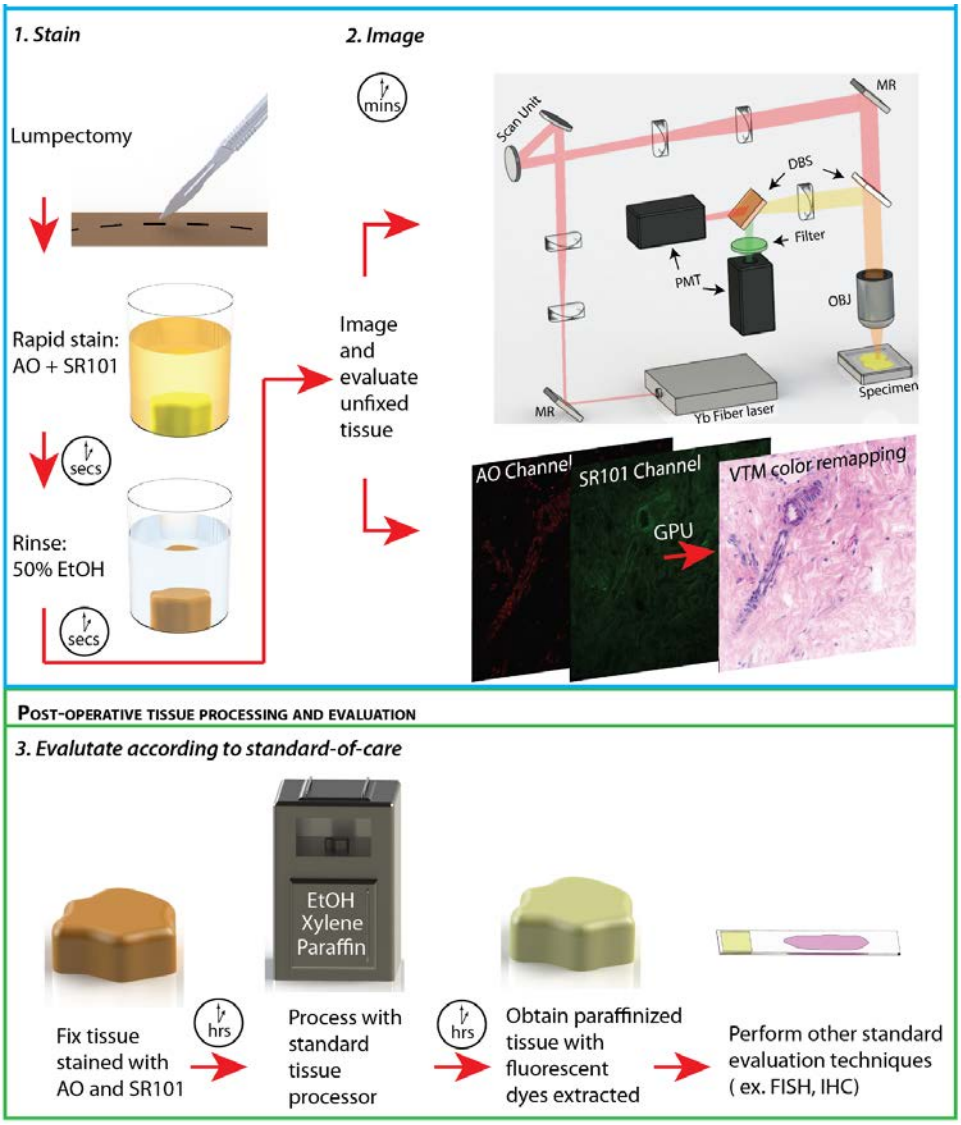

Figure 1. Nonlinear microscopy (NLM) for rapid histology. The specimens were transected, rapidly stained with AO and SR101, rinsed and placed on the nonlinear microscope stage. 10X and 20X objectives were used to visualize the tissue. The tissue was translated in the x, y, and z direction to examine the entire section of tissue (whole mount) up to 100 µm in depth (analogous to serial sectioning). A hematoxylin and eosin (H&E) like color image was generated using the AO and SR101 fluorescence signals. Stained tissue was formalin fixed and processed for standard paraffin embedded histology using a standard tissue processor, which includes ethanol dehydration, xylene rinsing, and paraffin infiltration. [L.C. Cahill, M.G. Giacomelli, T. Yoshitake, H. Vardeh, B.E. Faulkner-Jones, J.L. Connolly, C-K. Sun, and J.G. Fujimoto, "Rapid virtual hematoxylin and eosin histology of breast tissue specimens using a compact fluorescence nonlinear microscope," Lab. Invest. 98, 150-160, January 2018.]

We developed a video-rate computational light absorption model to generate realistic virtual H&E images of tissue in real time and in three dimensions. NLM imaging could be performed to depths of 100 µm below the tissue surface, which is important since many surgical specimens require subsurface evaluation due to artifacts on the surface from electrocautery, surgical ink or debris from specimen handling. We validated this method by subsequently processing NLM imaged specimens for paraffin embedded H&E histology, registering them to NLM images for pathology interpretation.

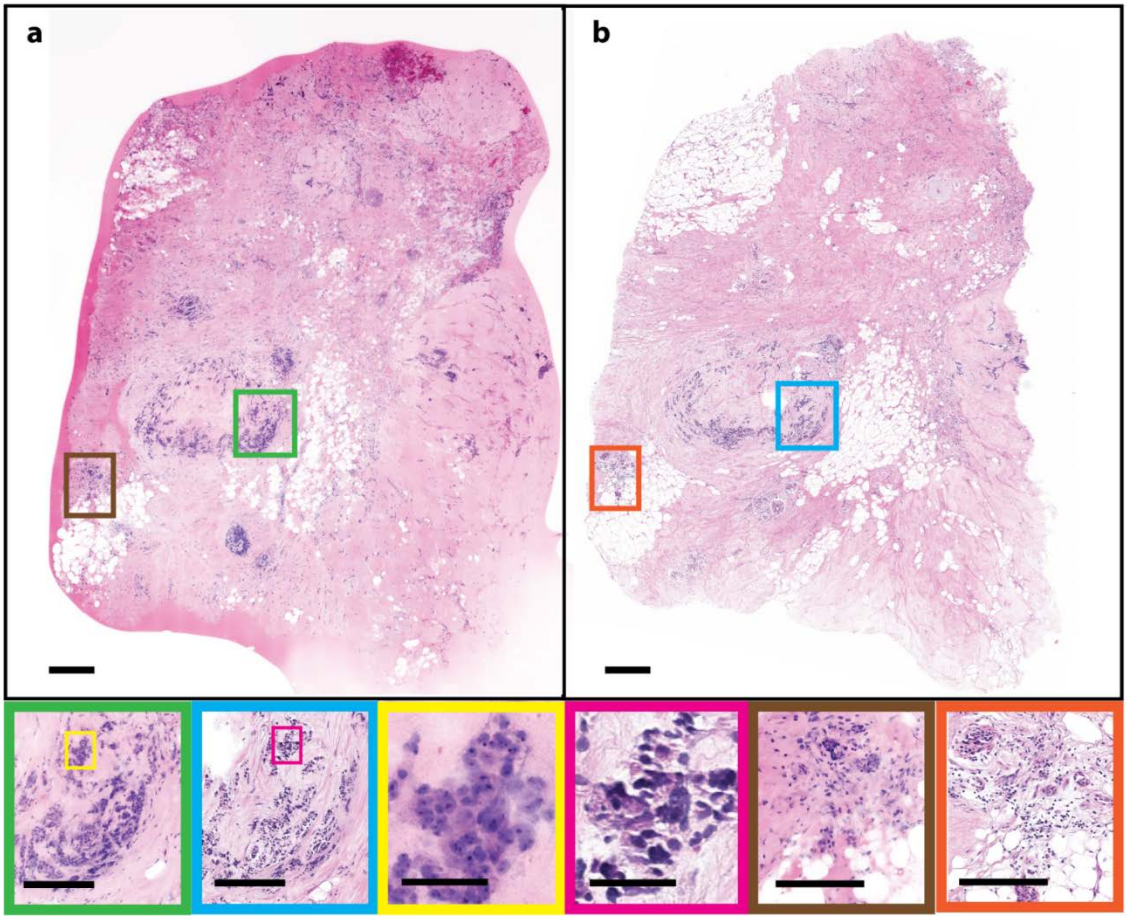

Figure 2. Human breast tissue showing invasive ductal carcinoma. (a) NLM and (b) formalin fixed paraffin embedded (FFPE) H&E images (500 µm scale bar). Malignant cells are shown in the NLM (green) and FFPE H&E images (blue) (250 µm scale bar) infiltrating the breast stroma, with a high magnification view shown in yellow (NLM) and pink (FFPE H&E) (50 µm scale bar); inflamed vessels with a lymphocytic infiltrate are shown in brown (NLM) and orange (FFPE H&E) (250 µm scale bar). NLM: https://slide-atlas.org/link/tfdr77. FFPE H&E: https://slide-atlas.org/link/zatgkv. [L.C. Cahill, M.G. Giacomelli, T. Yoshitake, H. Vardeh, B.E. Faulkner-Jones, J.L. Connolly, C-K. Sun, and J.G. Fujimoto, "Rapid virtual hematoxylin and eosin histology of breast tissue specimens using a compact fluorescence nonlinear microscope," Lab. Invest. 98, 150-160, January 2018.]

Rapid histology using NLM can have applications to breast as well as prostate cancer, two of the most common cancers in the female and male populations. Up to 30-40% of patients undergoing breast conserving surgery for breast cancer require repeat surgeries due to close or positive margins. The lengthy processing required for evaluating surgical margins by standard paraffin embedded histology precludes its use during surgery. FSA is faster, but only limited regions of the tissue can be imaged because of the need to freeze and cryosection specimens. Therefore, technologies for rapid evaluation of surgical margins could reduce the rates of repeat surgeries. Figure 2 shows a representative example of NLM imaging compared with standard formalin fixed paraffin embedded histology (FFPE) showing invasive ductal carcinoma. Diagnostically important features such as normal terminal ductal lobular units, fibrous and adipose stromal parenchyma, inflammation, invasive carcinoma, and in-situ lobular and ductal carcinoma were present in NLM images associated with pathologies identified on standard FFPE H&E histology. We also demonstrated that AO and SR101 were extracted to undetectable levels after FFPE processing and fluorescence in situ hybridization (FISH) HER2 amplification status was unaffected by the tissue processing and imaging methods.

It is important to note that NLM surgical margin evaluation can be performed in minutes, since comprehensive imaging of entire tissue cross sectional faces is rarely required. The edges of the tissue where surgical margins are represented as well as focal regions of interest can be rapidly assessed by translating the tissue under operator control and changing NLM objective magnifications. This operating mode would be comparable in speed to evaluating histology slides using a standard transmission light microscope, except that fresh, unsectioned tissue is imaged rather than paraffin embedded or frozen section stained slides.

Surgical margin assessment is also important in radical prostatectomy for prostate cancer. Positive margins can increase recurrence rates and the need for adjuvant radiation therapy. Although nerve sparing techniques reduce rates of post-operative incontinence and impotence, nerve sparing procedures are often not performed because of concerns that they will produce positive margins. Figure 3 shows a representative example of NLM imaging demonstrating the ability to image a multi-centimeter region of a freshly excised, unsectioned prostate cancer specimen.

We recently performed a study with 70 NLM and corresponding paraffin embedded H&E images of fresh and fixed prostate specimens (15 cancer, 55 benign) from 24 patients read by genitourinary pathologists to assess if NLM could achieve an equivalent evaluation to paraffin embedded H&E histology. Differences between NLM images and paraffin H&E slides, including cytoplasmic color and stromal density, were observed, however NLM images could be interpreted with minimal training. NLM enabled visualization of benign, atrophic and hyperplastic glands and stroma, ejaculatory ducts, vasculature and inflammatory changes. NLM enabled identification of typical and variants of adenocarcinoma as well as Gleason patterns. Perineural invasion and extraprostatic extension could also be assessed. Immunohistochemistry assays (p63, Prostate Specific Antigen, NKX3.1, Cytokeratin 34 beta E12, AMACR) were tested and found to be unaffected by NLM processing and imaging (data not shown) as expected since the fluorescent stains are removed to undetectable levels after standard histology processing.

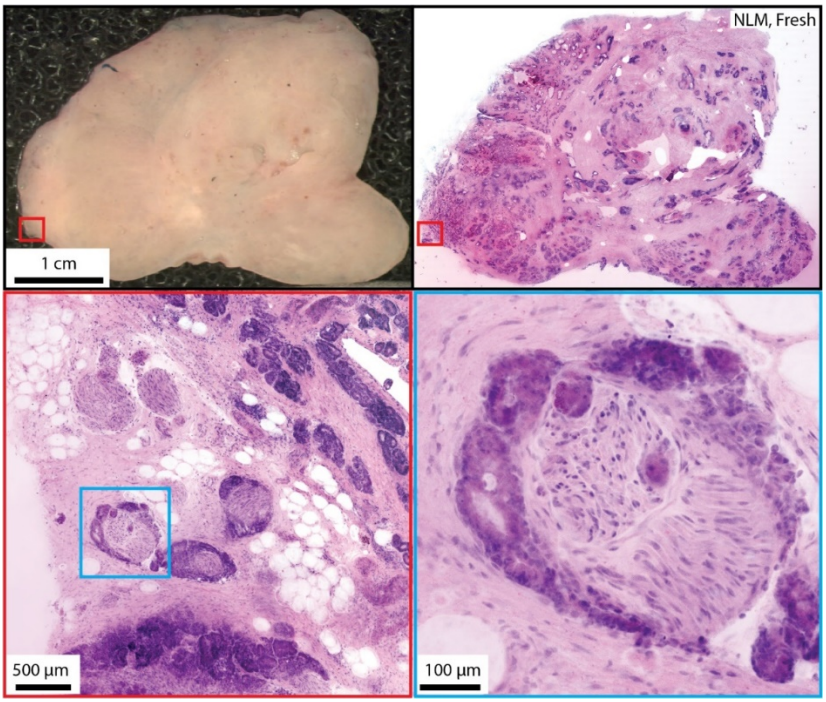

Figure 3. A white-light photograph and NLM image of multi-centimeter, freshly excised, unfixed prostate tissue. Extra-prostatic extension and perineural invasion is observed among the periprostatic fat (red and blue). (10x objective, 1 µm pixel). [L.C. Cahill, J.G. Fujimoto, M.G. Giacomelli, T. Yoshitake, D.I. Lin, H. Ye, O.M. Carrasco-Zevallos, A.A. Wagner, and S. Rosen, "Comparing histologic evaluation of prostate tissue using nonlinear microscopy and paraffin H&E: a pilot study," Mod. Pathol. In press.]

In contrast to FSA, NLM does not involve freezing and cryotoming, so large tissue specimens can be rapidly processed without requiring dissection into smaller sizes. Multiple tissue cross sections can be stained at one time and the pathologist can begin evaluation within ~2.5 minutes, while FSA requires each tissue cross section to be frozen in a separate block and individually cryotomed. Furthermore, NLM imaging can be performed up to 100 µm below the tissue surface. This capability is analogous serial sectioning in histology and provides visualization of depth resolved architectural morphology which can give additional insight into pathology or image below surface contaminants such as surgical debris. Finally, NLM is inherently digital which enables digital archiving and may facilitate future telepathology or computer-assisted diagnostic applications.

3. Dynamic light scattering optical coherence tomography (DLS-OCT) enables measurements of shear-induced diffusion of red blood cells

Dynamic light scattering (DLS) analysis uses the autocorrelation function of back scattered light to investigate the motion of particles. We integrated DLS with optical coherence tomography (DLS-OCT), which uses coherence gating to enable precise three-dimensional (3D) measurement of biophysical parameters at micrometer resolution. DLS-OCT can measure both blood flow

velocity and diffusion coefficient simultaneously, which are generally not differentiable using existing techniques such as laser Doppler flowmetry or conventional Doppler OCT.

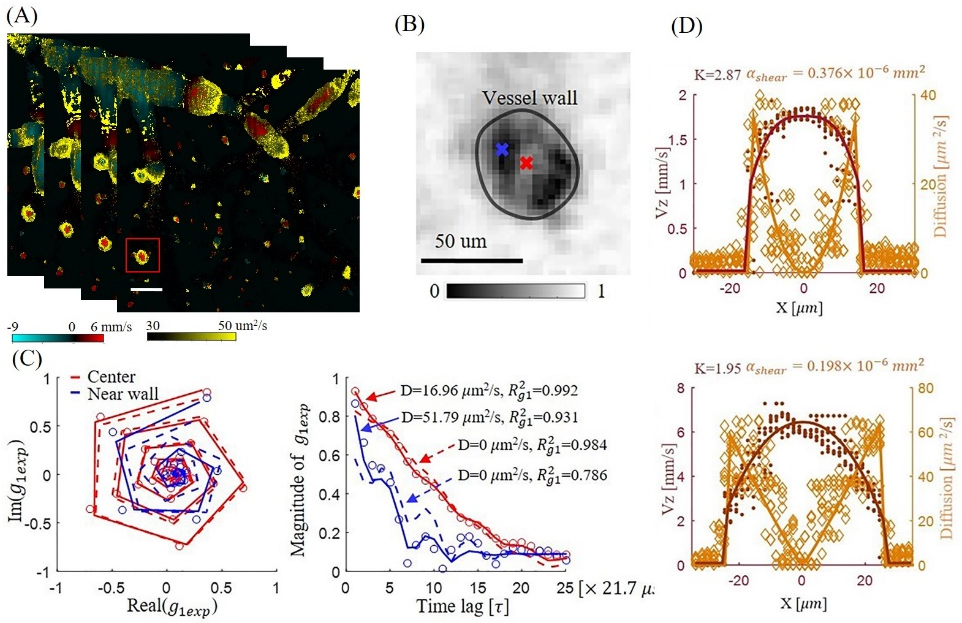

Figure 4. Simultaneous measurement of blood flow speed and diffusion coefficient. (A) *En face* single plane axial velocity overlapped with diffusion coefficient. The left and right color bars correspond to axial velocity and diffusion coefficient, respectively. (B) Experimental autocorrelation function (g_{1exp}) map at the 10th time lag for the ascending venule marked in (A). (C) Left: complex plane autocorrelation function curve at the center (red) and near wall (blue) positions within the vessel. Right: magnitude change of g_{1exp} versus time lag for the center (red) and near wall (blue) positions. Red and blue circles are the experimental g_{1exp}. Solid curves are the fitted results when considering both convective and diffusive motions of RBCs. The dashed curves illustrate the fitted results when only considering convective motion of RBCs (diffusion coefficient was set to 0). R^2_{g1} is the coefficient of determination, representing fitting accuracy. (D) Axial blood flow profile and diffusion coefficient profile of ascending venules with a vessel diameter of 31 μm (top) and 51 μm (bottom). Solid lines are the fitted laminar blood flow profile and diffusion coefficient profile of the averaged v_z and D along 10 profiles for each vessel section. Dark-red dots and orange diamonds represent the measured RBC velocity and diffusion coefficient along all 10 profiles, respectively [J. Tang, S. E. Erdener, B. Li, B. Fu, S. Sakadzic, S. A. Carp, J. Lee, and D. A. Boas, "Shear-induced diffusion of red blood cells measured with dynamic light scattering-optical coherence tomography," J. Biophotonics e201700070-, Aug 9 2017.]

We developed DLS-OCT for investigating rodent cerebral circulation in vivo demonstrating that it is possible to measure the axial and transverse components of the blood flow simultaneously and independently, providing absolute flow velocity measurement regardless of the Doppler angle. DLS-OCT can distinguish diffusive motion from translational flow, creating a separate 3D map of the diffusion coefficient to elucidate fluid transport in biological tissues including transport speed, radial profile, shear stress and shear-induced diffusion of blood cells. Translational flow velocity is related to systemic regulation of blood distribution from a macroscopic perspective

(macrocirculation), while diffusion determines the chemical exchange within the local region (microcirculation). These two biophysical processes are governed by different mechanisms, yet function synergistically to support the metabolic needs of organs. DLS-OCT can quantify and investigate behavior and interaction of the macro- and microcirculations, which is crucial to understanding the mechanisms of fluid transfer in living animals.

Using DLS-OCT, we studied blood flow shear rate and the shear-induced diffusion of red blood cells in rodents. This was the first *in vivo* study quantifying intravascular blood cell rheological behavior at microscopic level. Figure 4 shows the shear rate and shear-induced diffusion of red blood cells. Figure 4(C) shows the experimental autocorrelation function (g_{1exp}) decays faster near the vessel wall (blue) than in the center (red) implying a high shear-induced diffusion coefficient of red blood cells near the vessel wall consistent with RBC speed being slowest at the vessel wall. We also showed that in addition to convective motion, RBCs within the blood vessel also have diffusive motion; and that the diffusive motion is likely stronger (i.e. D is higher) near the vessel wall compared to the vessel center.

4. Capillary stalling measured with OCT angiography (OCTA)

Cerebral capillaries are the primary location where oxygen and nutrients exchange between the blood stream and local brain tissue. To investigate the microcirculation in physiology and disease, we need imaging approaches with both high spatial and temporal resolution. We applied OCT angiography (OCTA) time-series to detect and quantify transient interruptions in capillary flow caused by capillary red blood cell (RBC) stalls. Our approach permitted continuous imaging of ~200 capillaries for an extended period of time (up to 18 min) and with high temporal resolution (~0.1 Hz). Since OCTA is intrinsically sensitive to moving particles, exogenous labeling agents were not required.

We demonstrated that in mice, capillary flow was stalling intermittently, but consistently in a subset of monitored segments. These stalls were detectable as clear and sudden losses of OCTA signal, and could be manually marked at each time point (Fig. 5). We noted 7.50 ± 2.56% of all monitored capillaries had at least one stall in awake mice with chronic windows (n=7) during a 9-minute recording at resting conditions. At any instant, 0.45 ± 0.35% of capillaries were stalled. The average stall duration was ~15 seconds, but could last longer than 1 minute. Although each individual capillary stall was short-lasting, cumulatively, any given capillary segment that experienced a stall, had a cessation of flow for 5.8 ± 1.9% of the 9-minute observation time in awake, healthy mice. Stalls were more frequent and longer-lasting in anesthetized animals and following acute cranial window preparations (Incidence: 18.6 ± 8.7%, prevalence: 3.4 ± 1.5%, duration: 49.3 ± 21.1 seconds).

We performed whisker stimulation experiments (n=6) simultaneously with OCTA time-series measurements acquired over the barrel cortex in awake animals in order to assess whether capillary stalls would be affected by increased blood flow during functional activation. We compared stall incidences and point prevalence of stalls in the 5-frame-epochs before, during and after stimulation. Although stalls could still be observed during sensory stimulation, their average

incidence and prevalence were significantly lower during the stimulus than during the pre-stimulus period (Incidence: 1.27±0.68% vs 0.64±0.3% of all segments, p=0.018; Prevalence: 0.47±0.23% vs 0.2±0.09% of all segments, p=0.012; for pre-stimulus and stimulus, respectively). We hypothesize that this suggests an optimization of microcirculatory flow patterns for better tissue oxygenation during physiologically increased demand.

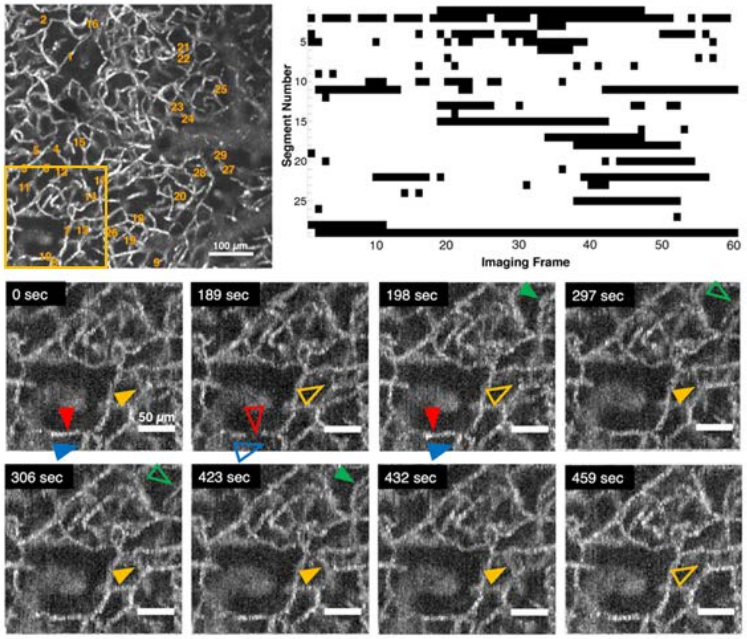

Figure 5. Representative OCTA images of capillary segments with stalling RBCs. Top left: Full field OCTA maximum intensity projection (150 to 250 µm below brain surface) with stalling segments indicated by numbers. Scalebar: 100 µm. Top right: Timeline of stalling segments through 60 consecutive images (~9 min). Black points denote stalls. Bottom: Individual segments (arrowheads) with temporary interruptions of RBC flux (zoom in of the ROI in the top-left image). Hollow arrowheads indicate a stalled capillary segment. Scalebar: 50 µm. [S. E. Erdener, J. Tang, A. Sajjadi, S. Kura, C. B. Schaffer, D. A. Boas. "Spatio-Temporal Dynamics of Cerebral Capillary Segments with Stalling Red Blood Cells," J Cerebr Blood F Met, Nov 2017.]

A systematic, quantitative approach for assessing capillary stalls creates new opportunities to study the complex microcirculation dynamics associated with disease. Future investigation should reveal the impact of stalls on oxygenation, even with normal pial arterial flow and a relatively normal capillary morphology. Our methods can be easily applied to different experimental models. Our goals for the next year include quantification of dynamic oxygenation changes in brain tissue near stalling capillary segments under baseline conditions and with functional activation. Repetitive, temporary fluctuations in tissue oxygen may have profound long term effects on the tissue. We are also planning to study whether pathologically increased amounts of capillary stalls in penumbra tissue of focal cerebral ischemia and in acute phase of traumatic brain injury correlate with tissue hypoxia and progressive cellular deterioration. This promises to provide information on the pathogenesis of traumatic brain injury and may facilitate strategies for its mitigation.

5. Capillary red blood cell velocimetry with phase resolved Doppler OCT (PR-DOCT)

The cerebral microcirculation is a complex vascular network that optimizes efficient delivery of oxygen for the high metabolic demand of the cerebral cortex. A precise measurement of capillary blood flow can complement the aforementioned studies of stochastic stalling of cerebral capillaries, providing more insight into the self-regulation of cerebral circulation. Unfortunately, this task is inherently challenging due to the small size of capillary vessels (around 5-10 μm), and the discontinuous, single-file nature of red blood cells (RBCs) flowing in capillaries.

We developed phase resolved Doppler OCT (PR-DOCT) techniques to enable accurate measurement of RBC speed in both large vessels and small capillaries. This method was based upon our observation that a continuous OCT phase shift can be detected from a single RBC moving in a capillary *in vivo*. To the best of our knowledge, no PR-DOCT technique has used this approach to obtain accurate RBC axial speed in capillaries (<10 μm in size).

Figure 6 shows a representative OCTA image and axial capillary RBC speed map obtained with PR-DOCT. This method measured RBC axial speed in most capillaries (67 out of 84 vessel segments). To verify the measured RBC speed, we compared the measured total speed ($v_z/\cos(\theta)$, where θ is the angle between the vessel and the optical beam axis, obtained from the corresponding OCTA) with the RBC passage speed (assuming an RBC diameter of $5\,\mu m$) from 50 randomly selected locations where RBC passage could be identified. As shown in Fig. 6(C), the speed measured by the RBC induced phase shifts correlated with the speed measured by the RBC passage, and the regression line had a slope of 1.08 (with intercept forced to 0) indicating similar quantitative values for the RBC speed. The difference from the expected unity slope is likely a result of an error in the assumed diameter of the RBC and in the estimation of vessel angle.

We also studied the effect of the number of A-line repetitions (n_t) on the RBC speed measurement. As shown in Fig. 6(D), the larger the n_t (longer repeated acquisition time) the better quality of the RBC axial speed image. In particular, the measurements in capillaries with slow RBC speeds were greatly improved with increased measurement repetitions. We also calculated the ratio of the number of non-zero v_z pixels for different A-line repetitions versus that of 800 A-line repetitions in order to quantitatively assess the impact of a reduced number of A-line repetitions (Fig. 6(E)). We believe $n_t = 50$ A-line repetitions (Interscan time $\Delta t = 1.05\,\mathrm{ms}$ for each A-line location) provides an acceptable trade-off between measurement duration and image quality. This corresponds to a total acquisition time of ~45 s for a volumetric 3D capillary RBC speed measurement spanning 200 × 200 pixels laterally. We focused at 3 different depths to acquire 3 volumetric images and then combined them to form the axial speed image across the entire cerebral cortex layer. Figure 6(F) demonstrates that the RBC axial speed in large vessels and small capillaries was successfully detected across the whole cortex. The PR-DOCT-based capillary velocimetry method will serve as a foundation for our future studies of brain disease, such as stroke, Alzheimer's disease and aging.

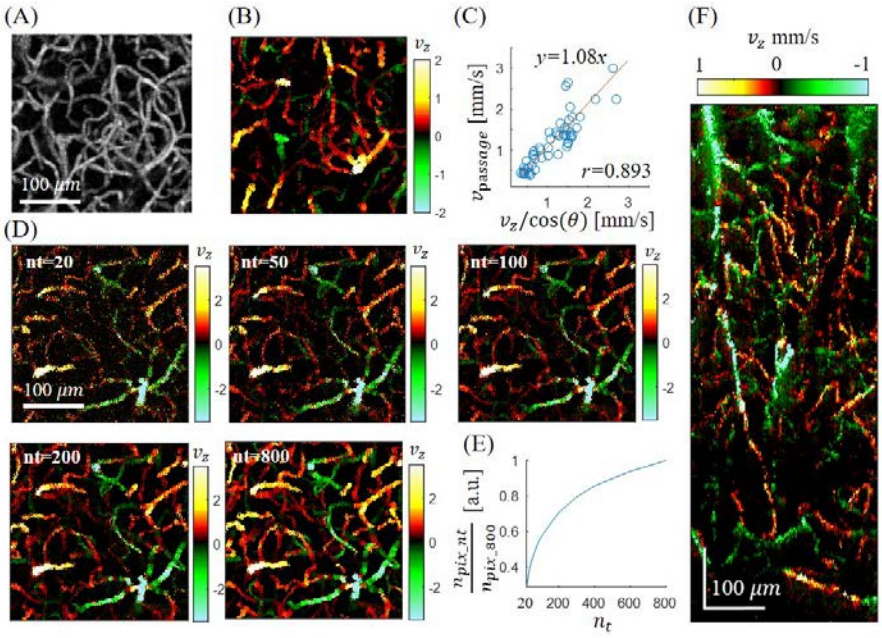

Figure 6. (A) OCTA maximum intensity projection (MIP) spanning a depth of 170 to 330 μm from the cortical surface. (B) v_z MIP maps over the same depth range as (A). (C) Comparison between the measured axial speed ($v_z/\cos(\theta)$, where θ is the angle of the vessel) and the RBC passage speed ($v_{passage}$) from 50 randomly selected locations. (D) Results from mouse #2 showing the improvement with an increasing number of repeated A-scans (n_t) on capillary velocimetry ($\Delta t =$ 0.42 ms, 1.05 ms, 2.1 ms, 4.1 ms, and 16.8 ms corresponding to $n_t =$ 20, 50, 100, 200, and 800, respectively), *en face* X-Y v_z MIP maps were obtained over the depth range of 100 to 265 μm from the cortical surface. (E) Ratio of the number of v_z pixels for different A-line repetitions divided by that of $n_t = 800$. (F) X-Z MIP (~100 μm stack along Y) of axial speed across the whole cerebral cortex obtained from mouse #3. Color bar: axial blood flow speed (mm/s); Positive value: blood flows toward brain surface; Negative value: blood flows into brain. No spatial filtering was applied to the results. [J. Tang, S. E. Erdener, B. Fu, and D. A. Boas. "Capillary Red Blood Cell velocimetry by Phase-resolved Optical Coherence Tomography," Opt Lett, vol. 42, pp. 3976-3979, Sep 2017.]

6. Visualizing vasculature and blood flow in the human retina using variable interscan time analysis (VISTA) OCTA and ultrahigh speed OCTA

Working with collaborators at the New England Eye Center (NEEC) have developed and applied optical coherence tomography angiography (OCTA) techniques to study biophysical processes in the retina. This research translates methods developed for studies in the small animal brain to investigations in the human retina. In particular, we have developed techniques for measuring changes in retinal capillary blood flow speed due to disease as well as neurovascular coupling. OCTA can visualize vasculature by acquiring repeated OCT B-scans, comparing the repeated B-scans, and generating a motion contrast image which detects flowing blood (Fig. 7). OCTA has several features which make it a powerful technique for research: (1) In contrast to fluorescein angiography (FA) or indocyanine green angiography (ICG), it can visualize microvasculature

without requiring dye injection. (2) Imaging can be performed repeatedly, when FA or ICG would not be warranted, (3) OCTA images are depth resolved enabling visualization of the different retinal capillary plexi as well as the choriocapillaris and choroid which are below the retina and retinal pigment epithelium.

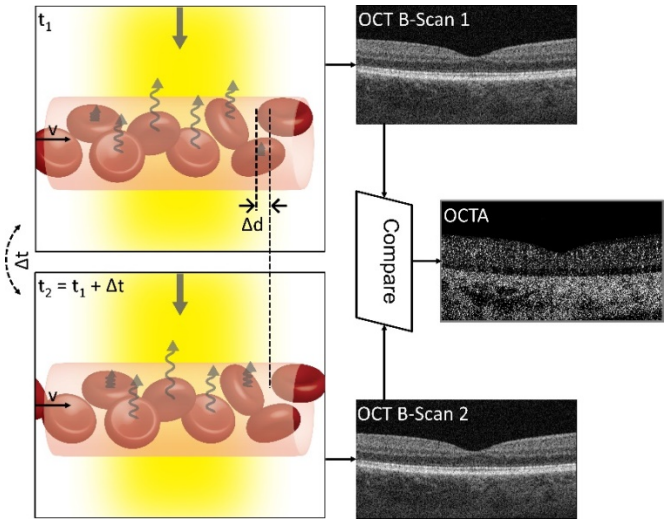

Figure 7. Principles of optical coherence tomography angiography (OCTA). Two or more OCT B-scans are acquired at the same retinal location: one at time t_1, and the other at time t_2, separated by Δt (the interscan time). Tissue regions without moving blood cells will generate an identical OCT signal at times t_1 and t_2; however, regions containing flowing blood cells will generate different OCT signals at time t_1 and time t_2 – due to the displacement of the blood cells $\Delta d \approx v \cdot \Delta t$, where v is the blood cell speed. By comparing repeated OCT B-scans and extracting the time-varying components, an OCTA image of the vasculature can be computed.

Although OCTA yields information about the presence or absence of blood flow, it provides limited information about blood flow speeds. The dynamic range of standard OCT used in retinal imaging is very limited so that flow impairment can be difficult to detect. This contrasts to techniques such as DLS-OCT and PR-DOCT discussed earlier in the report, which give absolute measurements of blood flow speeds, but are challenging to use in the human retina due to the longer scan times required. To address these challenges and extend OCTA to relative blood flow measurements, our group developed a technique called variable interscan time analysis (VISTA). The interscan time, the time between repeated OCT B-scans (Δt), plays a critical role in determining the relationship between the blood flow speed and measured OCTA signal, with different interscan times capturing different blood flow information (Fig. 8). VISTA exploits the OCTA signal dependency on interscan time, using it to deduce relative blood flow speeds. Long interscan times which are used in commercial ophthalmic OCTA instruments are sensitive to slow flows but cannot detect variations in faster flows. Using shorter interscan times, sensitivity to slow flows are reduced, but it is possible to detection variations in fast flows, flow impairment.

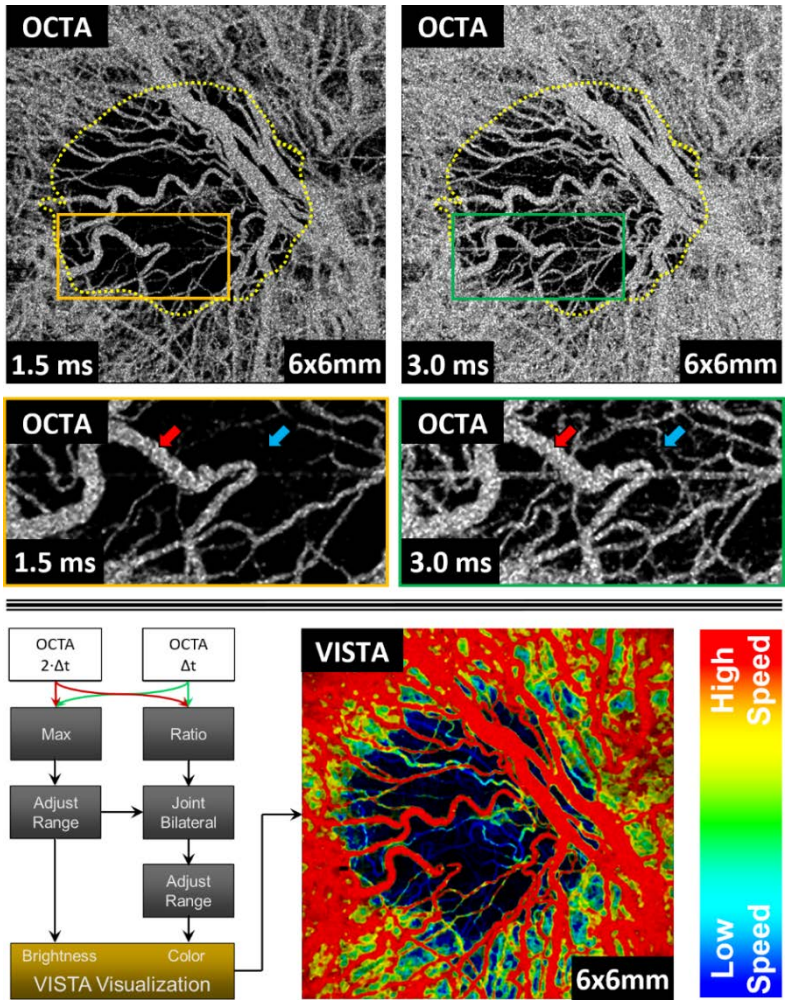

Figure 8. Variable interscan time analysis (VISTA). (Top) Effect of interscan time on *en face* OCTA images in a patient with age related macular degeneration and geographic atrophy (dashed yellow contour demarcates a region of atrophy). The left images were 1.5 ms interscan time OCTA, whereas the right images were 3.0 ms interscan time OCTA. Enlargements of the orange and green boxes reveal that certain vessels (blue arrow) are visible in the 3.0 ms interscan time OCTA image but not in the 1.5 ms interscan time OCTA image. Other vessels (red arrow) are visible in both the 3.0 ms and 1.5 ms interscan time OCTA images. This implies that the blood flow in the vessel indicated by the blue arrow is too slow to generate an OCTA signal in the 1.5 ms interscan time image; demonstrating that the blood flow in the vessel indicated by the blue arrow is slower than the blood flow in the vessel indicated by the red arrow. This example demonstrates how blood flow speeds can be inferred by comparing OCTA images formed using variable interscan times. (Bottom) These observations can be formalized and the 1.5 ms interscan time (Δt) and 3.0 ms interscan time images ($2 \cdot \Delta t$) mapped into a color-coded VISTA image, where red and blue indicating faster and slower flow. [S. B. Ploner, E. M. Moult, W. Choi, N. K. Waheed, B. Lee, E. A. Novais, E. D. Cole, B. Potsaid, L. Husvogt, J. Schottenhamml, A. Maier, P. J. Rosenfeld, J. S. Duker, J. Hornegger, and J. G. Fujimoto, "Toward Quantitative Optical Coherence Tomography Angiography: Visualizing Blood Flow Speeds in Ocular Pathology Using Variable Interscan Time Analysis," Retina, Sep 28 2016.]

OCTA and VISTA requires the rapid acquisition of multiple OCT B-scans with short interscan times (less than ~3 ms), therefore high speed OCT technology is required. Working in collaboration with Thorlabs and Praevium Research, we have developed ultrahigh speed swept source OCT (SS-OCT) using vertical cavity surface emitting laser technology. We have performed extensive studies using SS-OCT at 400 kHz A-scan rates, 4-5x faster than commercial OCT technology. Figure 8 shows an example of VISTA OCTA from a patient with age related macular degeneration and geographic atrophy. Figure 9 shows an example of functional imaging in the human retina where blood flow speed increases in response to flicker stimulation.

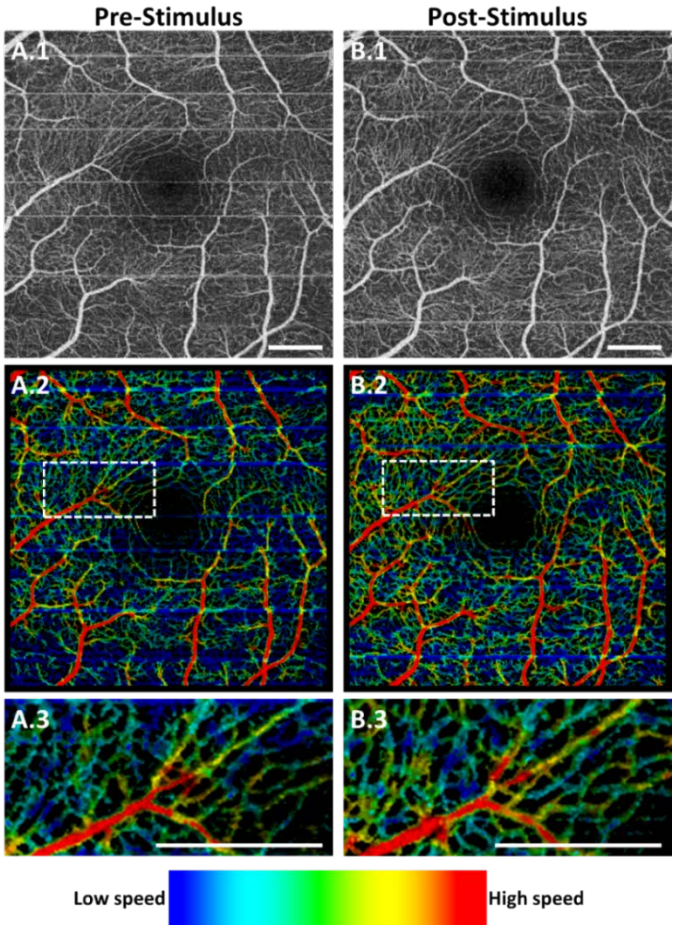

Figure 9. Effect of flicker light stimulus on blood flow speed in a normal human retina (29-year-old male subject). (A) Pre-stimulus image and (B) post-stimulus image at 45 seconds after continuous exposure to an 8-Hz flicker stimulus. Top row shows standard OCTA images of the total retinal vasculature, computed with a 1.5-ms interscan time. Middle row shows corresponding VISTA images. Bottom row shows enlargements of the dashed white boxes of the middle row. Retinal blood flow speeds are increased post-stimulus. Extensions of this technique will enable functional neurovascular response to be imaged and measured within depth resolved individual capillary layers of the retina as well as at different positions across the retina. All scale bars are 500-μm.

Recently we have increased SS-OCT imaging speeds to 800 kHz A-scan rates, up to 10x faster than commercial instruments. These high speeds enable OCTA with very short interscan times (less than 1 ms) which enable subtle differences in blood flow to be detected. The high speeds also enable time resolve OCTA using repeated volumetric acquisition to resolve dynamic changes in blood flow. Figure 10 shows an example of time resolved OCTA at rates of 6 volumes per second acquired in a patient with age related macular degeneration and geographic atrophy. OCTA signals from the intermediate size and smaller vessels vary as a function of cardiac cycle. Larger vessels appear constant because flow speed is high and the OCTA signal is saturated.

The impairment of blood flow, capillary loss and ischemia are thought to play a critical role in the pathogenesis both age related macular degeneration and diabetic retinopathy. The ability to detect the impairment of blood flow at a treatable stage, before loss of vasculature occurs, would accelerate fundamental studies on disease pathogenesis as well as improve the ability to track disease progression and response to therapy. We have developed ultrahigh speed SS-OCT technology which in use at the New England Eye Center for studies of disease mechanisms in patients.

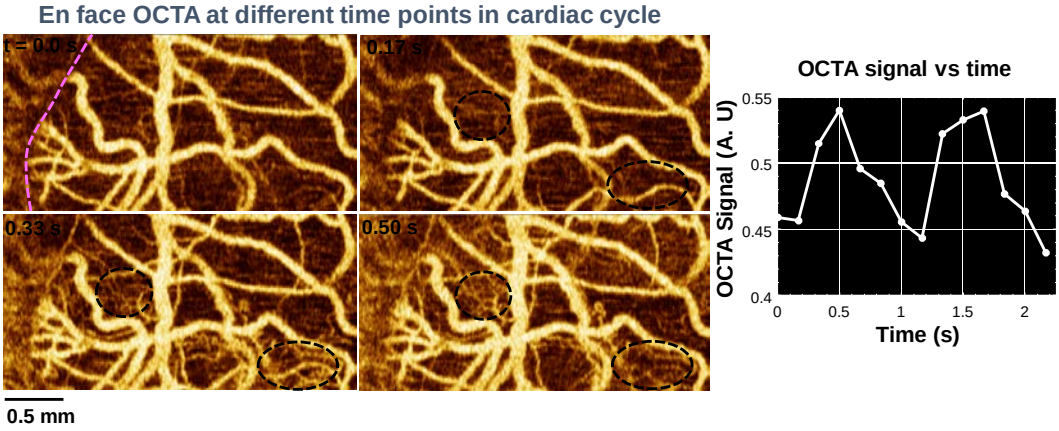

Figure 10. OCT using ultrahigh speed SS-OCT at 800 kHz A-scan rate enables the detection of subtle changes in blood flow as well as time resolved OCTA using repeated volumetric acquisition to visualize dynamic processes. Representative time resolved OCTA using 500 A-scans per B-scan and 2 repeated B-scans with an interscan time of 0.835 ms. A 6 Hz or 12 Hz volumetric imaging speed can be achieved using 100 or 50 B-scan rasters. OCTA from a patient with age related macular degeneration and geographic atrophy. Images over a 3 mm x 1.5 mm field of view at 6 Hz show the choriocapillaris and choroidal vasculature at the margin of geographic atrophy. Heart rate is measured with a pulse oximeter. OCTA images are displayed using a hue rather than grey scale in order to improve visualization of signal variations.

7. Investigating photoreceptor and retinal pigment epithelium function in humans using ultrahigh resolution spectral domain OCT (UHR-OCT)

We have developed new imaging techniques for monitoring photoreceptor and retinal pigment epithelium (RPE) function using ultrahigh resolution (UHR) spectral domain OCT (UHR-OCT).

These techniques can map photoreceptor and RPE function across the retina and promise to enable new fundamental as well as clinical research. The photoreceptor outer segments (OS) are the locus of visual phototransduction, generating neural signals in response to light stimulation (Fig. 11). Lipid bilayer membranes within the photoreceptor OS are densely packed with photopigments, G-protein-coupled receptor proteins (GPCRs). Upon absorbing light of appropriate wavelength, these photosensitive receptor proteins undergo conformational changes, activating the G-protein cascade, leading to amplification of the stimulus signal and transduction. In the human retina, the rhodopsin-rich rod receptors are responsible for phototransduction of monochromatic vision in low light and photopsin-rich cone receptors for color vision in brighter lit environments.

Chemical conformational changes shift the photopigment absorption spectra such that they no longer respond to visible light stimulation and are “bleached”. The activated pigments must then be restored to their original conformation before they can be excited again. This recovery process involves transporting bleached pigment toward the retinal pigment epithelium (RPE), isomerizing bleached rhodopsin and photopsin back to their original, photosensitive configuration, and transporting them back to the outer segments of the photoreceptors. This is a rate-limiting process governed by enzymatic kinetics and resistive diffusion. Figure 12 shows a hydraulic analogy to illustrate the linear arrangement of this process, showing the photopigment rhodopsin recovery dynamics. We have developed imaging techniques to assess these fundamental processes to measure functional alterations in the photoreceptors and RPE occurring in aging and disease.

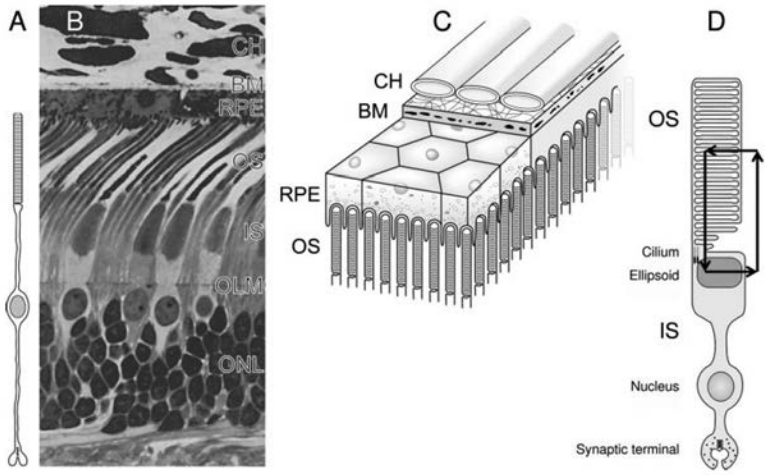

Figure 11. Anatomical features of the outer retina, retinal pigment epithelium (RPE), and photoreceptors. (A) Schematic of mammalian rod photoreceptor and (B) Microscopy image of the parafoveal region in the rhesus monkey showing choroid, RPE, and distal retina. (C) Schematic of choriocapillaris, Bruch’s membrane, retinal pigment epithelial cells, and tips of the rod outer segments. (D) Schematic of an amphibian rod, showing the circulating current. CH, choriocapillaris; BM, Bruch’s membrane; RPE, retinal pigment epithelium; OS, outer segments; IS, inner segments; OLM, outer limiting membrane; ONL, outer nuclear layer. [Figure reprinted from Lamb and Pugh, Phototransduction, Dark Adaptation, and Rhodopsin Regeneration, *Invest. Ophth. Vis. Sci*. **47**, 2006.]

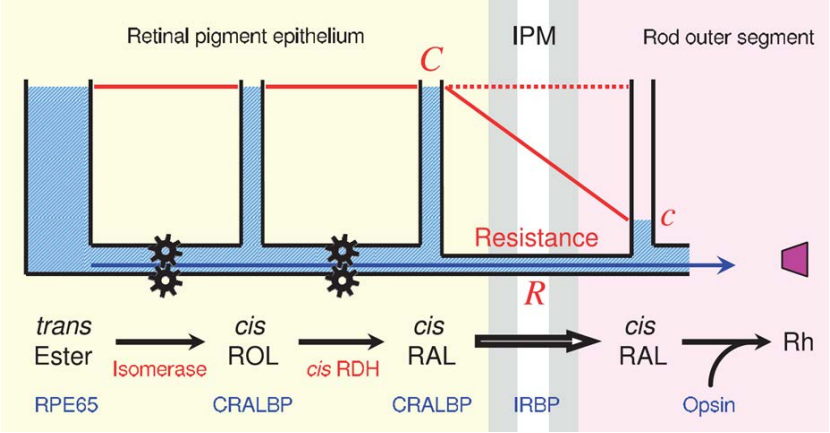

Figure 12. Hydraulic analogy of rate limitation in retinoid delivery. The height of each fluid column represents the "concentration" of retinoid species in the relevant compartments (RPE or outer segment), and the cogs represent enzymatic conversion steps. In the fully dark-adapted state, when no opsin is present, there is no flux of retinoid out of the system (i.e., the exit pipe is plugged), and the fluid column heights will be equal. (Heights have been scaled according to the reaction equilibrium constants.) When opsin is produced after exposure to light (photobleaching), the local concentration c of 11-*cis* retinal in the outer segment drops, and retinoid (modelled as fluid) flows as a result of the pressure difference, $C - c$. In the case shown, the flow limitation is assumed to be the resistance R to delivery of 11-*cis* retinal to opsin in the outer segments. It is also possible for the limitation to occur at either of the two preceding enzymatic steps. In the hydraulic analogy this is modelled as one of the first two horizontal pipes being very narrow. Each of these scenarios generates closely resembles rate-limited kinetics of retinoid delivery. [Figure reprinted from Lamb and Pugh, Phototransduction, Dark Adaptation, and Rhodopsin Regeneration, *Invest. Ophth. Vis. Sci.* **47**, 2006.]

In the normal retina, rhodopsin recovers after a total bleach within approximately 30 minutes, while the recovery of photopsin is much faster. The light-sensitivity of the eye is temporarily decreased (the activation threshold is increased) and this delayed recovery of photosensitivity is referred as dark adaptation. Studies have shown that dark adaptation recovery dynamics are related to the light exposure, with slower recovery associated with higher beach levels. Dark adaptation consists of two distinct regimens. The first regimen consists of a rapid sensitivity recovery associated with photopsin-rich cone photoreceptors, which occurs during the first few minutes of dark adaptation and ends in a plateau. The second regimen is a gradual sensitivity recovery of rhodopsin-rich rod photoreceptors. Rod recovery begins ~15 minutes after removal of light stimulation in healthy subjects, and can require up to an hour depending on the bleach level. The dynamics corresponds well with the biophysical and biochemical alterations within photoreceptors following light stimulus. Therefore, quantitative measurement of dark adaptation can be a useful tool for investigating the transduction mechanisms and function of the retina and RPE. Furthermore, dark adaptation is impaired by retinal disease and patients with age-related macular degeneration (AMD) have prolonged or compromised dark adaptation. Thus, quantifying dark adaptation dynamics can characterize fundamental biophysical processes in the photoreceptors and RPE, as well as assess function as a potential marker for pharmaceutical treatment. Traditional dark adaptation studies require subjects to respond to varying levels of light stimuli to measure

sensitivity changes. These techniques can have high variability and only a limited number of positions across the retina can be measured. Quantitative imaging techniques which map function across the retina are needed.

Working in collaboration with Prof. Edward Pugh (University of California Davis), an expert on phototransduction, we have developed OCT imaging techniques and structural markers for underlying biophysical and biochemical process characterizing dark adaptation sensitivity recovery. Dr. Pugh's group and others have shown that changes in the permeability of membrane ion channels occur during phototransduction and the subsequent fluid flow leads to detectable swelling of the photoreceptor cells. We have developed UHR-OCT methods to quantify the ~100 nm class thickness changes in the rod and cone photoreceptors and RPE in the human retina.

The UHR-OCT instrument used a 870 nm center wavelength and 170 nm full-width half-maximum (FWHM) bandwidth to achieve a 3 μm FWHM axial resolution in tissue (4 μm in air) at ~90 kHz A-scan rate. Figure 13(A) shows a representative structural UHR-OCT from a healthy subject. Five bright bands can be identified in the outer retina in the cross-sectional image (Fig. 13). From anterior to posterior, these five bands are interpreted as the (1) ellipsoid zone (EZ), also referred as inner segment/outer segment junction (IS/OS); (2) cone interdigitation zone (CIZ) or cone outer segment tips (COST); (3) rod interdigitation zone (RIZ) or cone outer segment tips (ROST); (4) RPE; and (5) Bruch's membrane (BM). The OCT structural bands were segmented and their relative distances to the EZ(IS/OS) band measured to characterize photoresponse of the cones, rods and RPE.

Light exposure / bleaching protocols were used to investigate the dark adaptation sensitivity recovery process in the human retina. The retina was exposed to a flash of 528 nm light with calibrated exposures so that 23%, 54%, and 96% of the rhodopsin was bleached. After the light exposure, we acquired UHR-OCT volumes at ~20-second intervals over the initial five minutes to observe early-phase rapid response and then every five minutes until 30 minutes after exposure to investigate the long-term response.

The dynamic change in the thickness from EZ (IS/OS) to CIZ (COST) was statistically significant at 54% and 96% bleach levels, while EZ-RIZ (IS/OS-ROST), EZ-RPE (IS/OS-RPE), EZ-BM (IS/OS-BM) thickness changes were statistically significant for all bleach levels (general linear mixed model analysis). Additionally, one subject was measured with a traditional dark adaptometer along with UHR-OCT in order to confirm the expected bleaching levels and dark adaptation behavior. The dynamics of the EZ-CIZ (IS/OS-COST) response was similar to that of cone sensitivity recovery in dark adaptometry, while the EZ-RIZ (IS/OS-ROST) response was similar to that of rod sensitivity recovery (Fig. 14).

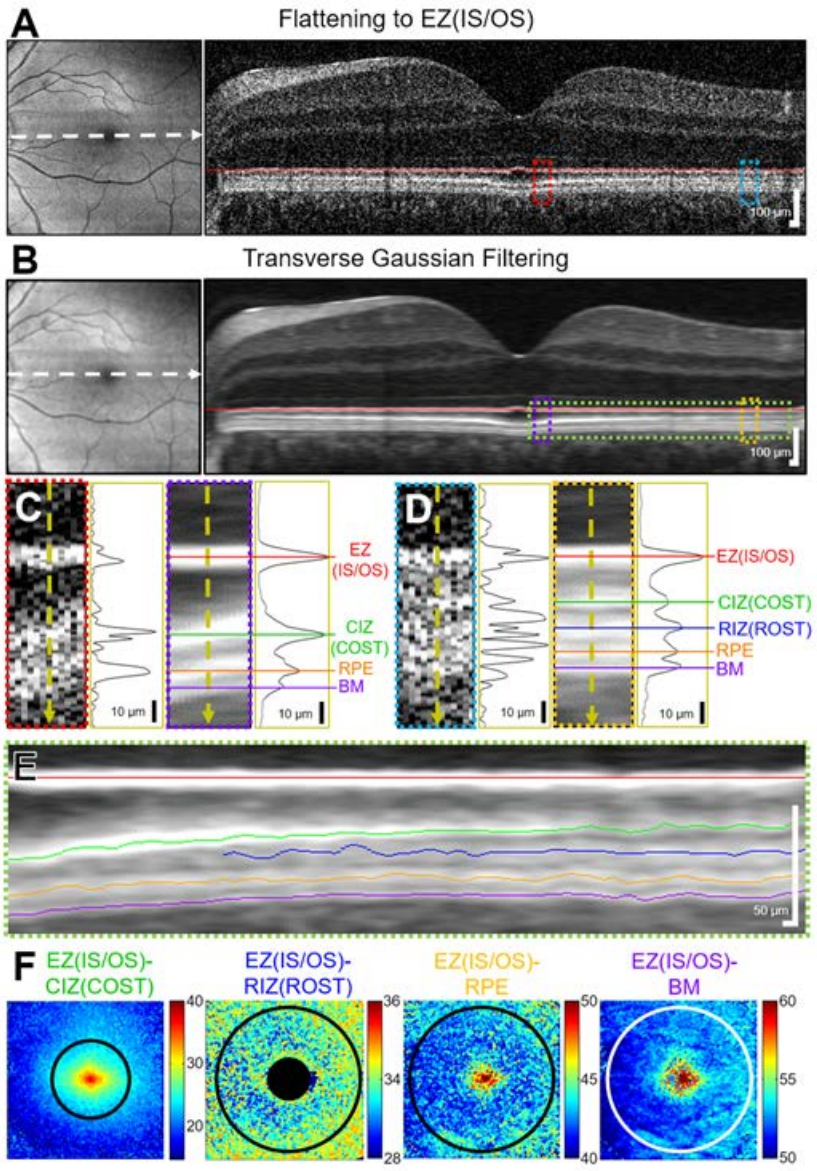

Figure 13. Imaging processing for OCT volumes acquired at each timepoint. En face projection and log-scale single B-scans are flattened to the ellipsoid zone (EZ) inner segment / outer segment (IS/OS) junction. (A) Flattened 6 mm x 6 mm, 400 x 400 A-scan volume before and (B) after 2D transverse Gaussian filtering at every axial depth in the volume. Enlargement of the B-scan and a single linear-scale A-scan (C) near and (D) peripheral to the foveal pit show OCT features of the outer retina after transverse filtering. The resolvable outer retinal bands are the cone interdigitation zone (CIZ), also known as the cone outer segments (COST); rod interdigitation zone (RIZ), or rod outer segment tips (ROST); apical retinal pigment epithelium (RPE); and the Bruch's membrane (BM). (E) The outer retinal bands are identified by intensity peak detection colored segmentation lines overlaid on the B-scans. (F) Application of the peak detection to all B-scans produces a thickness map for the four bands relative to the EZ(IS/OS). Numbers associated with the colored lines give depths in micrometers relative to the EZ(IS/OS).

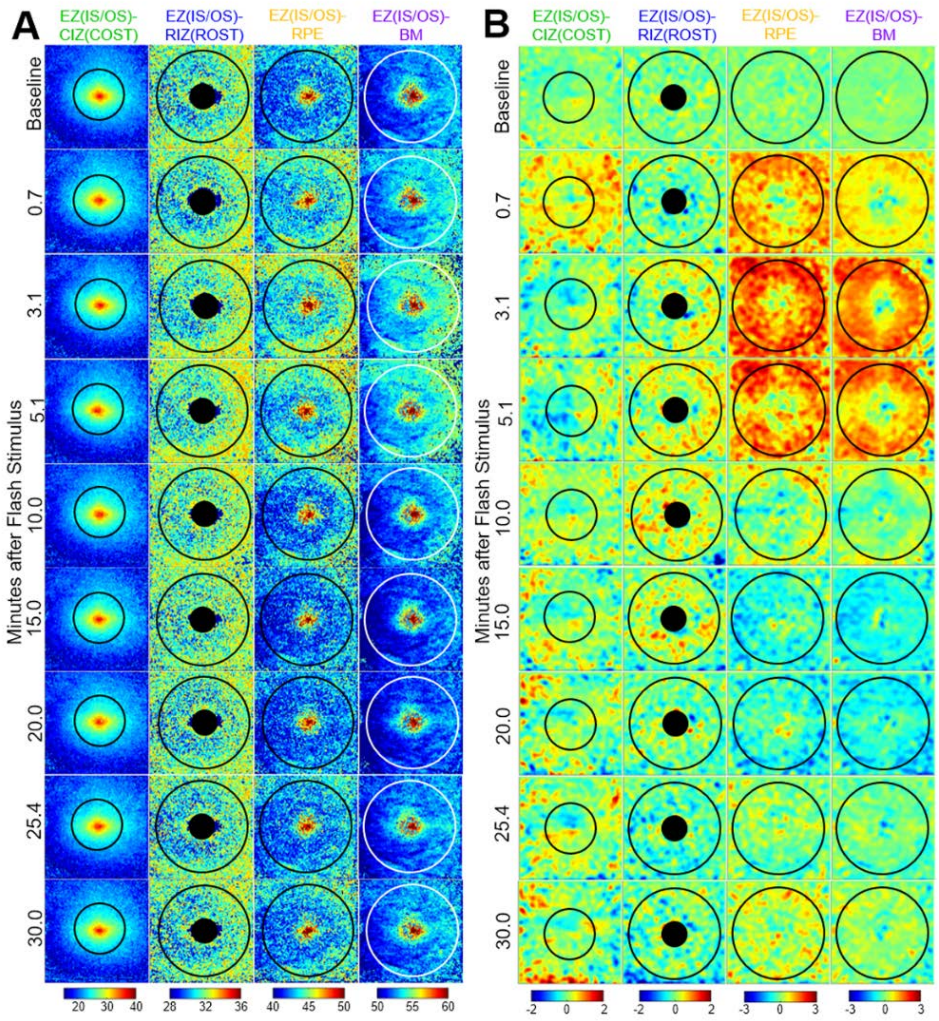

Figure 14. (A) Selected thickness map time points from a single subject before and after a 96% full field rhodopsin bleach. The color bars give depths in micrometers relative to the EZ. (B) Thickness difference maps between each time point and averaged baseline. A 2D Gaussian filter with sigma = 9 A-scans was applied to the thickness difference maps. [C. D. Lu, B. Lee, J. Schottenhamml, A. Maier, E. N. Pugh, Jr., and J. G. Fujimoto, "Photoreceptor Layer Thickness Changes During Dark Adaptation Observed With Ultrahigh-Resolution Optical Coherence Tomography," Invest Ophthalmol Vis Sci, vol. 58, pp. 4632-4643, Sep 1 2017.]

Spatially averaged thickness changes within a 5.5 mm diameter area in each subject confirm the observations from the thickness difference maps and show the dynamic response of the photoreceptors (Fig. 15). Structural changes required 100-nm level differences to be detected. The EZ-RIZ (IS/OS-ROST) sharply increased in the first few minutes after the light exposure and then gradually returned to baseline between 10 to 20 minutes after exposure. This coincides with the time range of rod sensitivity recovery observed in traditional dark adaptometry and suggests that these measurements can be used as a surrogate for dark adaptation. Other OCT studies of photoreceptors in light and darkness with frogs and mice have also detected changes in the retinal outer segments. We believe the underlying mechanism osmolarity driven flow of ionic compounds

into the RPE following exposure to light. Thus UHR-OCT imaging can measure ion transport phenomena, which is a marker for photoreceptor and RPE function.

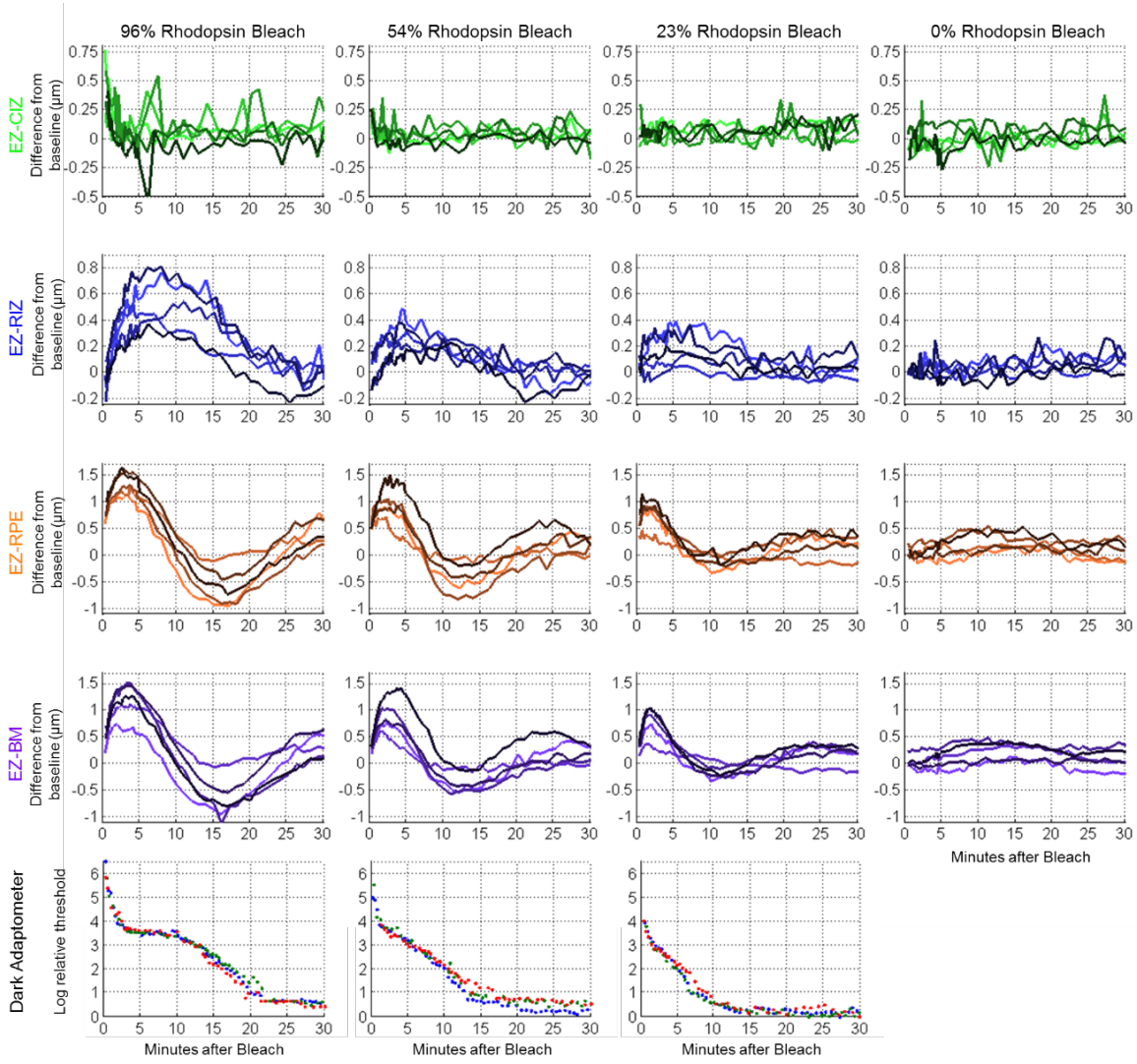

Figure 15. UHR-OCT averaged thickness map area differences (photoresponses) from baseline in 5 subjects for full-field 96%, 54%, 23% and 0% rhodopsin bleaches. At the bottom, the results from three sessions using the dark adaptometer on one subject with the same bleach protocol at 96%, 54%, and 23% rhodopsin bleaches are plotted to compare against the UHR-OCT results. Thickness changes are small and require measurement noise levels to be reduced to the ~100 nm scale. These results suggest that precision structural measurements can map cone, rod and RPE function. [C. D. Lu, B. Lee, J. Schottenhamml, A. Maier, E. N. Pugh, Jr., and J. G. Fujimoto, "Photoreceptor Layer Thickness Changes During Dark Adaptation Observed With Ultrahigh-Resolution Optical Coherence Tomography," Invest Ophthalmol Vis Sci, vol. 58, pp. 4632-4643, Sep 1 2017.]

The distances from EZ (IS/OS) to RPE and to BM both had a more complex, oscillatory behavior, resembling the step response of an underdamped second order system. Similar dynamics have been shown in the electroretinogram (ERG) and electrooculogram (EOG) literature. This dynamic

response warrants further investigation and could also shed light on the underlying biophysics of chemical transport and function of photoreceptors and RPE.

We have recently built a next generation UHR SD-OCT instrument using a new, high speed line scan CMOS camera in combination with high speed delay scanning to extend imaging range. This instrument achieves 3 um axial resolution in tissue with up to 250 kHz A-scan rate, 2-3x faster than previous UHR instruments. We are also developing image processing including software motion correction and graph-cut segmentation methods to improve the thickness measurement accuracy. This should reduce noise and enable functional response to be measured within finer regions across the retina. We are also investigating variable inter-scan time analysis OCT angiography (VISTA-OCTA) in the choriocapillaris (the dense capillary bed beneath BM) during light exposure. Measurements of blood flow could yield complementary information on photoreceptor and RPE function, providing a comprehensive technique to assess the earliest changes in retinal aging and disease.

8. Other accomplishments of co-principal investigators

This section summarizes accomplishments of the co-PIs during the program.

Honorary Doctorate from the Friedrich-Alexander-Universitat Erlangen-Nuremberg (2018)
James Fujimoto received an Honorary Doctorate from the Faculty of Engineering at the Friedrich-Alexander-Universitat Erlangen-Nuremberg, Germany in a ceremony held in January 2018. This was in recognition of a long standing collaboration with Prof. Joachim Hornegger, President of the University, in the field of medical image processing and training exchange students.
https://www.tf.fau.eu/2018/02/general/honorary-doctorate-awarded-to-professor-james-fujimoto-ph-d/

National Academy of Engineering Russ Prize 2017
James Fujimoto was co-recipient of the National Academy of Engineering Russ Prize along with Mr. Eric Swanson (from MIT), Prof. Christoph Hitzenberger and Prof. Adolf Fercher (Medical University of Vienna) – For optical coherence tomography, leveraging creative engineering to invent imaging technology essential for preventing blindness and treating vascular and other diseases. The Russ Prize is a $500,000 prize awarded biannually and recognizes an outstanding bioengineering achievement in widespread use that improves the human condition.
https://www.nae.edu/Projects/Awards/RussPrize.aspx
https://www.nae.edu/Activities/Projects/Awards/RussPrize/RussWinners.aspx
https://www.youtube.com/watch?v=FyXZZveuCUA&t=0s&index=27&list=PLJ8uEbBRJZKeLEmqvvZ49gabLb60-Ie4l

European Inventor Award 2017
James Fujimoto was co-recipient of the European Inventor Award in the non-EPO category along with Mr. Eric Swanson (MIT) and Prof. Robert Huber (University of Lubeck). The award is selected by a jury based not only on technological originality, but also on economic and social impact.
https://www.epo.org/learning-events/european-inventor/finalists.html
https://www.epo.org/learning-events/european-inventor/finalists/2017/fujimoto.html

Beckman Argyros Award in Vision Research 2017
James Fujimoto also received the Beckman-Argyros Award in Vision Research. The Beckman-Argyros Award is a $500,000 award to one individual annually who has made and is continuing to make significant transformative breakthroughs in vision research; particularly through the development of an innovative technology or fundamental scientific breakthrough that has been applied to, aided and/or improved the vision sciences.
http://www.beckman-foundation.org/beckman-news/2017BeckmanArgyrosAward

Dr. Boas appointed Founding Director of Boston University Neurophotonics Center
David Boas has joined Boston University as well as having a joint appointment at Harvard Medical School and Massachusetts General Hospital. He became the founding director at the Boston University Neurophotonics Center. Allied with the existing Photonics Center, the newly created department seeks to build and support an interdisciplinary community that can pioneer and translate impactful photonics technologies in the field of neuroscience. These innovations are driving profound advances in understanding brain phenomena such as electrical excitability,

neuroglial partnership, neurovascular signaling, metabolic activity, and hemodynamics. The center will not only contribute to our knowledge on how the brain works in health, but will also accelerate the understanding of brain disease and injury, as well as guide new diagnostic and therapeutic strategies.
https://www.bu.edu/today/2017/neurophotonics-center/
http://www.bu.edu/neurophotonics/

25th Anniversary of OCT Review
Eric Swanson (MIT) and James Fujimoto co-authored an invited paper for a special issue of Biomedical Optics Express (2017) commemorating the 25th anniversary of the invention of optical coherence tomography. The paper "The ecosystem that powered the translation of OCT from fundamental research to clinical and commercial impact" describes the history of OCT development and commercialization as well as its economic impact.
https://www.osapublishing.org/boe/abstract.cfm?uri=boe-8-3-1638

$9 Billion Healthcare savings from OCT
A 2018 study showed that Optical Coherence Tomography (OCT) resulted in a $9 billion in savings in health care costs over an eight year period from more efficient use of the pharmaceuticals to treat Age Related Macular Degeneration. OCT was developed by our group at MIT and collaborators in the 1990s and this study is an example of the long term impact of research. Two of the co-authors (D. Huang and E. Swanson) are collaborators. Dr. Huang is a former Harvard-MIT, MD-PhD student. ["Estimating Public and Patient Savings From Basic Research - A Study of Optical Coherence Tomography in Managing Antiangiogenic Therapy", Matthew A. Windsor, Sissi J.J. Sun, Kevin D. Frick, Eric A. Swanson, Philip J. Rosenfeld, David Huang, American Journal of Ophthalmology 185, 122 (2018)]
http://www.octnews.org/articles/7491596/new-study-finds-federally-funded-technology-saved-/
http://www.ajo.com/article/S0002-9394(17)30419-1/fulltext

9. Publications under AFOSR Award FA9550-15-1-0473

This section reports publications under this program as well as publications from the translation and application of technologies and methods developed which cite AFOSR sponsorship.

[1] E.M. Moult, A.Y. Alibhai, C. Rebhun, B. Lee, S. Ploner, J. Schottenhamml, L. Husvogt, C.R. Baumal, A.J. Witkin, A. Maier, J.S. Duker, P.J. Rosenfeld, N.K. Waheed, and J.G. Fujimoto, "Spatial distribution of choriocapillaris impairment in eyes with choroidal neovascularization secondary to age-related macular degeneration: A quantitative OCT angiography study," Retina. In press.

[2] L.C. Cahill, J.G. Fujimoto, M.G. Giacomelli, T. Yoshitake, D.I. Lin, H. Ye, O.M. Carrasco-Zevallos, A.A. Wagner, and S. Rosen, "Comparing histologic evaluation of prostate tissue using nonlinear microscopy and paraffin H&E: a pilot study," Mod. Pathol. In press.

[3] O.O. Ahsen, K. Liang, H.-C. Lee, M.G. Giacomelli, Z. Wang, B.M. Potsaid, and J.G. Fujimoto, "Assessment of Barrett's esophagus and dysplasia with ultrahigh-speed volumetric en face and cross-sectional optical coherence tomography," Endoscopy 50, 1-12, September 2018.

[4] R.F. Spaide, J.G. Fujimoto, N.K. Waheed, S.R. Sadda, and G. Staurenghi, "Optical coherence tomography angiography," Prog. Retin. Eye Res. 64, 1-55, May 2018.

[5] A.Y. Alibhai, E.M. Moult, R. Shahzad, C.B. Rebhun, C. Moreira-Neto, M. McGowan, D. Lee, B. Lee, C.R. Baumal, A.J. Witkin, E. Reichel, J.S. Duker, J.G. Fujimoto, and N.K. Waheed, "Quantifying microvascular changes using OCT angiography in diabetic eyes without clinical evidence of retinopathy," Ophthalmol. Retina 2, 418-427, May 2018.

[6] M.G. Giacomelli, T. Yoshitake, L.C. Cahill, H. Vardeh, L.M. Quintana, B.E. Faulkner-Jones, J. Brooker, J.L. Connolly, and J.G. Fujimoto, "Multiscale nonlinear microscopy and widefield white light imaging enables rapid histological imaging of surgical specimen margins," Biomed. Opt. Exp. 9, 2457-2475, May 2018.

[7] C.B. Rebhun, E.M. Moult, S.B. Ploner, C. Moreira-Neto, A.Yasin Alibhai, J. Schottenhamml, B. Lee, W. Choi, F.A. Rifai, M.W. Tam, L. Husvogt, C.R. Baumal, A.J. Witkin, A. Maier, P.J. Rosenfeld, J.S. Duker, J.G. Fujimoto, and N.K. Waheed, "Analyzing relative blood flow speeds in choroidal neovascularization using variable interscan time analysis OCT angiography," Ophthalmol. Retina 2, 306-319, April 2018.

[8] T. Yoshitake, M.G. Giacomelli, L.M. Quintana, H. Vardeh, L.C. Cahill, B.E. Faulkner-Jones, J.L. Connolly, D. Do, and J.G. Fujimoto, "Rapid histopathological imaging of skin and breast cancer surgical specimens using immersion microscopy with ultraviolet surface excitation," Sci. Rep. 8, 4476, March 2018.

[9] C.D. Lu, N.K. Waheed, A. Witkin, C.R. Baumal, J.J. Liu, B. Potsaid, A. Joseph, V. Jayaraman, A. Cable, K. Chan, J.S. Duker, and J.G. Fujimoto, "Microscope-integrated intraoperative ultrahigh-speed swept-source optical coherence tomography for widefield retinal and anterior segment imaging," Ophthalmic Surg. Lasers Imaging Retina 49, 94-102, February 2018.

[10] L.C. Cahill, M.G. Giacomelli, T. Yoshitake, H. Vardeh, B.E. Faulkner-Jones, J.L. Connolly, C-K. Sun, and J.G. Fujimoto, “Rapid virtual hematoxylin and eosin histology of breast tissue specimens using a compact fluorescence nonlinear microscope,” Lab. Invest. 98, 150-160, January 2018.

[11] K. Liang, Z. Wang, O.O. Ahsen, H.-C. Lee, B.M. Potsaid, V. Jayaraman, A. Cable, H. Mashimo, X. Li, and J.G. Fujimoto, “Cycloid scanning for wide field optical coherence tomography endomicroscopy and angiography in vivo,” Optica 5, 36-43, January 2018.

[12] S. E. Erdener, J. Tang, A. Sajjadi, S. Kura, C. B. Schaffer, D. A. Boas. "Spatio-Temporal Dynamics of Cerebral Capillary Segments with Stalling Red Blood Cells," J Cerebr Blood F Met, Nov 2017.

[13] J. Tang, S. E. Erdener, B. Fu, and D. A. Boas. "Capillary Red Blood Cell velocimetry by Phase-resolved Optical Coherence Tomography," Opt Lett, vol. 42, pp. 3976-3979, Sep 2017.

[14] J. Tang, S. E. Erdener, B. Li, B. Fu, S. Sakadzic, S. A. Carp, J. Lee, and D. A. Boas. "Shear-induced Diffusion of Red Blood Cells Measured with Dynamic Light Scattering – Optical Coherence Tomography," J Biophotonics, e20170070, Aug 9, 2017.

[15] E. A. Swanson and J. G. Fujimoto, "The ecosystem that powered the translation of OCT from fundamental research to clinical and commercial impact [Invited]," Biomedical Optics Express, vol. 8, pp. 1638-1664, Mar 1 2017.

[16] E. M. Moult, W. Choi, D. A. Boas, B. Baumann, A. C. Clermont, E. P. Feener, and J. G. Fujimoto, "Evaluating anesthetic protocols for functional blood flow imaging in the rat eye," Journal of Biomedical Optics, vol. 22, Jan 2017.

[17] C. D. Lu, B. Lee, J. Schottenhamml, A. Maier, E. N. Pugh, Jr., and J. G. Fujimoto, "Photoreceptor Layer Thickness Changes During Dark Adaptation Observed With Ultrahigh-Resolution Optical Coherence Tomography," Invest Ophthalmol Vis Sci, vol. 58, pp. 4632-4643, Sep 1 2017.

[18] K. Liang, O. O. Ahsen, Z. Wang, H. C. Lee, W. Liang, B. M. Potsaid, T. H. Tsai, M. G. Giacomelli, V. Jayaraman, H. Mashimo, X. Li, and J. G. Fujimoto, "Endoscopic forward-viewing optical coherence tomography and angiography with MHz swept source," Opt Lett, vol. 42, pp. 3193-3196, Aug 15 2017.

[19] H. C. Lee, O. O. Ahsen, J. J. Liu, T. H. Tsai, Q. Huang, H. Mashimo, and J. G. Fujimoto, "Assessment of the radiofrequency ablation dynamics of esophageal tissue with optical coherence tomography," J Biomed Opt, vol. 22, p. 76001, Jul 1 2017.

[20] H. C. Lee, O. O. Ahsen, K. Liang, Z. Wang, M. Figueiredo, M. G. Giacomelli, B. Potsaid, Q. Huang, H. Mashimo, and J. G. Fujimoto, "Endoscopic optical coherence tomography angiography microvascular features associated with dysplasia in Barrett's esophagus (with video)," Gastrointest Endosc, vol 86, pp. 476-484, Feb 5 2017.

[21] B. Lee, E. A. Novais, N. K. Waheed, M. Adhi, T. E. de Carlo, E. D. Cole, E. M. Moult, W. Choi, M. Lane, C. R. Baumal, J. S. Duker, and J. G. Fujimoto, "En Face Doppler Optical Coherence Tomography Measurement of Total Retinal Blood Flow in Diabetic Retinopathy and Diabetic Macular Edema," JAMA Ophthalmol, vol. 135, pp. 244-251, Mar 1 2017.

[22] E. D. Cole, E. M. Moult, S. Dang, W. Choi, S. B. Ploner, B. Lee, R. Louzada, E. Novais, J. Schottenhamml, L. Husvogt, A. Maier, J. G. Fujimoto, N. K. Waheed, and J. S. Duker, "The Definition, Rationale, and Effects of Thresholding in OCT Angiography," Ophthalmol Retina, vol. 1, pp. 435-447, Sep-Oct 2017.

[23] W. Choi, N. K. Waheed, E. M. Moult, M. Adhi, B. Lee, T. De Carlo, V. Jayaraman, C. R. Baumal, J. S. Duker, and J. G. Fujimoto, "Ultrahigh Speed Swept Source Optical Coherence Tomography Angiography of Retinal and Choriocapillaris Alterations in Diabetic Patients with and without Retinopathy," Retina, vol. 37, pp. 11-21, Jan 2017.

[24] B. Li, H. Wang, B. Fu, R. Wang, S. Sakadžić, D. A. Boas, "Impact of temporal resolution on estimating capillary RBC-flux with optical coherence tomography," J Biomed Opt, vol. 22, pp. 016014, January 26 2017.

[25] T. Yoshitake, M. G. Giacomelli, L. C. Cahill, D. B. Schmolze, H. Vardeh, B. E. Faulkner-Jones, J. L. Connolly, and J. G. Fujimoto, "Direct comparison between confocal and multiphoton microscopy for rapid histopathological evaluation of unfixed human breast tissue," J Biomed Opt, vol. 21, p. 126021, Dec 1 2016.

[26] J. Schottenhamml, E. M. Moult, S. Ploner, B. Lee, E. A. Novais, E. Cole, S. Dang, C. D. Lu, L. Husvogt, N. K. Waheed, J. S. Duker, J. Hornegger, and J. G. Fujimoto, "An Automatic, Intercapillary Area-Based Algorithm for Quantifying Diabetes-Related Capillary Dropout Using Optical Coherence Tomography Angiography," Retina, Sep 13 2016.

[27] S. B. Ploner, E. M. Moult, W. Choi, N. K. Waheed, B. Lee, E. A. Novais, E. D. Cole, B. Potsaid, L. Husvogt, J. Schottenhamml, A. Maier, P. J. Rosenfeld, J. S. Duker, J. Hornegger, and J. G. Fujimoto, "Toward Quantitative Optical Coherence Tomography Angiography: Visualizing Blood Flow Speeds in Ocular Pathology Using Variable Interscan Time Analysis," Retina, Sep 28 2016.

[28] E. M. Moult, N. K. Waheed, E. A. Novais, W. Choi, B. Lee, S. B. Ploner, E. D. Cole, R. N. Louzada, C. D. Lu, P. J. Rosenfeld, J. S. Duker, and J. G. Fujimoto, "Swept-Source Optical Coherence Tomography Angiography Reveals Choriocapillaris Alterations in Eyes with Nascent Geographic Atrophy and Drusen-Associated Geographic Atrophy," Retina, Sep 30 2016.

[29] K. Liang, O. O. Ahsen, H. C. Lee, Z. Wang, B. M. Potsaid, M. Figueiredo, V. Jayaraman, A. E. Cable, Q. Huang, H. Mashimo, and J. G. Fujimoto, "Volumetric Mapping of Barrett's Esophagus and Dysplasia With en face Optical Coherence Tomography Tethered Capsule," Am J Gastroenterol, vol. 111, pp. 1664-1666, Nov 2016.

[30] J. Lee, Y. Gursoy-Ozdemir, B. Fu, D. A. Boas, and T. Dalkara, "Optical coherence tomography imaging of capillary reperfusion after ischemic stroke," Appl Opt, vol. 55, pp. 9526-9531, October 2016.

[31] H. C. Lee, O. O. Ahsen, K. Liang, Z. Wang, C. Cleveland, L. Booth, B. Potsaid, V. Jayaraman, A. E. Cable, H. Mashimo, R. Langer, G. Traverso, and J. G. Fujimoto, "Circumferential optical coherence tomography angiography imaging of the swine esophagus using a micromotor balloon catheter," Biomed Opt Express, vol. 7, pp. 2927-42, Aug 1 2016.

[32] M. G. Giacomelli, L. Husvogt, H. Vardeh, B. E. Faulkner-Jones, J. Hornegger, J. L. Connolly, and J. G. Fujimoto, "Virtual Hematoxylin and Eosin Transillumination Microscopy Using Epi-Fluorescence Imaging," PLoS One, vol. 11, p. e0159337, Aug 8 2016.